CRUSTAL STRUCTURE BENEATH HI-CLIMB SEISMIC ARRAY IN WESTERN TIBETAN PLATEAU FROM A GENERALIZED H-K METHOD

BY

FANGRUO ZHAO

THESIS

Submitted in partial fulfillment of the requirements
for the degree of Master of Science in Geology
in the Graduate College of the
University of Illinois at Urbana-Champaign, 2018

Urbana, Illinois

Advisers:

Professor Xiaodong Song
Associate Professor Lijun Liu

ABSTRACT

Receiver function(RF) is commonly used for analyzing seismic waves generated at structural boundaries and imaging major interfaces of the Earth. The traditional *H-κ* method using grid search and RF stacking developed by Zhu and Kanamori (2000) has been applied for calculating H and κ of the crust globally. Accurate crustal thickness (H) and average crustal Vp/Vs ratio (κ) are essential for understanding the tectonic setting and other fundamental geological questions. However, the traditional *H-κ* method may provide some questionable results in regions where crustal structures are complex and uncertain, like crustal anisotropy and dipping crust. Recently, *H-κ* method with harmonic corrections, which corrects both Ps and crustal multiples by including crustal azimuthal anisotropy and dipping interfaces for multiple layers, was developed by Jiangtao Li, Xiaodong Song, and Pan Wang at the University of Illinois. We apply this new method to the dense Hi-CLIMB seismic array in western-central Tibetan Plateau, which covered Yarlung-Zangpo Suture (YZS) and Bangong-Nujiang Suture (BNS) linearly along approximately 85°E. With the improved H value, we can better interpret both past and present tectonic settings of the region, as improved κ value can offer better constraints for mineral composition and melting condition of the crust.

To My Parents

ACKNOWLEDGMENTS

I sincerely thank my advisor, Prof. Xiaodong Song for his continuous and tireless support and guidance during my graduate study at the University of Illinois. I appreciated his valuable suggestions both on my research and career, and his supports on my decisions. Also I thank my co-advisor, Prof. Lijun Liu, for his endless help during my graduate study, and his careful work on my thesis. Additionally, I thank my group members, namely Jing Jin, Jiangtao Li, Yi Yang, Zheng Chen, Pan Wang, and Hongyu Xiao, for their assistances and discussions on my research. Thanks to Dr. Pan Wang and Jiangtao Li for providing the *H*-κ method with harmonic corrections program. Also thanks to Prof. Lupei Zhu and his students for providing the data. Finally, thanks to my parents and girlfriend who have accompanied, supported, and encouraged me to go through each step through my master program.

TABLE OF CONTENTS

CHAPTER 1: INTRODUCTION

Tibetan Plateau, the highest and largest plateau on Earth, was formed by the collision between the Indian Plate and Eurasian Plate after the closure of Tethys ocean in the early Cenozoic (Nabelek et al., 2009). The structures of the Tibetan Plateau continuously alter since the development of the Cenozoic Tibetan Plateau in the Eocene (Patriat and Achache, 1984). The Main Boundary Thrust (MBT) serves as the surface boundary between these two continental plates. The Tibetan Plateau is composed of several microplates, which are separated by sutures with the presence of ophiolitic materials. The Yarlung-Zangpo Suture (YZS) and Bangong-Nujiang Suture (BNS) separate the Tibetan Plateau into Himalaya Block (HB), Lhasa Block (LB), and Qiangtang Block (QB) from south to north (Fig. 1.). The BNS was formed around the late Triassic to early Jurassic, and the YZS was later formed in early Tertiary due to the collision (Dewey et al., 1988).

The Moho discontinuity is the most distinguished velocity conversion which separates the crust from the mantle. Accurate location of the Moho can provide important constraints to understand the mantle lithosphere structure and mechanism of the collision. Seismologists have been studied the structures beneath this region for a few decades. Most of the studies were focused on the eastern side of the plateau (Zhang et al., 2011), leaving the western part of the plateau less well understood. The Hi-CLIMB (Himalaya-Tibetan Continental Lithosphere During Mountain Building) seismic array in the western Tibetan Plateau was deployed from 2002 to 2005 which covers most of the major features (Fig. 1).

Many seismological methods have been used to study the region from the seismic data of Hi-CLIMB. The traditional H-κ stacking method of Zhu and Kanamori (2000) which calculates the depth of Moho discontinuity and the Vp/Vs ratio beneath a seismic array by stacking the receiver functions of teleseismic P-wave sources are widely used. Wittlinger et al. (2009) suggested that

the crustal thickness is approximately 78 km beneath LB, and 70 km depth beneath Q by combining both S-to-P and P-to-S receiver function methods. The high shear velocities and low Vp/Vs ratio are interpreted as eclogite layer of the deep Indian lower crust. Nabelek et al., (2009) also used receiver function method and suggested that the crust and Moho discontinuity are anisotropic. The weak Moho Ps conversion from in LB and southern QB suggest that the region is highly deformed. The waveform modeling study of Tseng et al. (2009), the Gaussian-beam migration of scattered teleseismic P-wave study of Nowack et al. (2010), shows a northward thinning crust from 75 km thick in the HB to over 60 km thick in QB with complex structure beneath BNS. These two studies also observed similar Moho variation beneath LB. Xu and Song (2013) proposed a joint inversion method using surface wave dispersion data and receiver function data. The study suggests the similar result of Moho depth with previous studies, but the low shear velocity zones indicate partial melting beneath LB from 29.4°N to 31°N beneath QB from 31.5°N to 33.5°N.

With the dipping Moho and crustal anisotropy in Tibetan Plateau, the traditional H-κ method that assumes flat Moho and the isotropic crust may produce uncertain or even unrealistic results. The generalized H-κ method with Harmonic correction (cHκ) is proposed to correct the effects before the stacking (Li et al., 2018, submitted). In this study, we apply this method to teleseismic P-wave radial receiver functions (R-RF) recorded by Hi-CLIMB seismic array. The near N-S oriented linear array can provide great 2-D Moho depth profile and Vp/Vs ratio profile across the Tibetan Plateau.

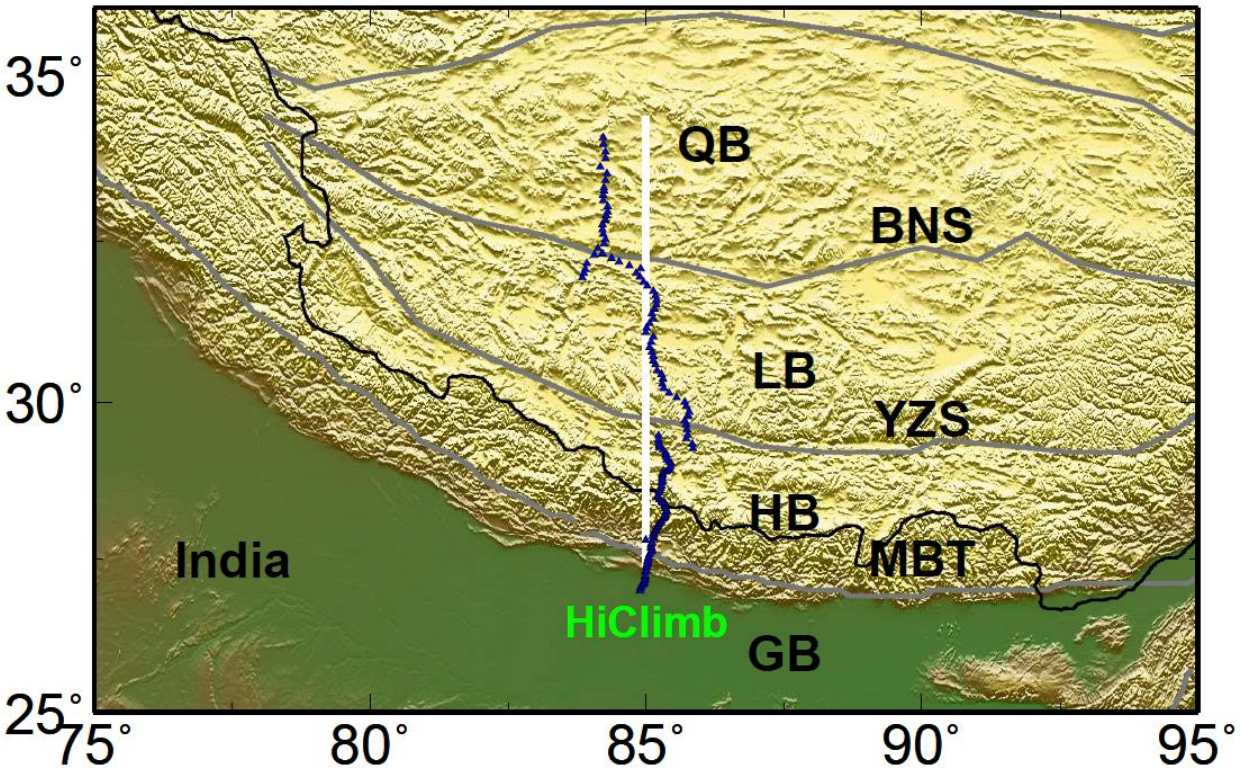

Figure 1.1: Major tectonic blocks of the Tibetan Plateau and Hi-CLIMB seismic array station distribution (blue triangles). The grey lines mark the boundaries of major blocks including Main Boundary Thrust (MBT), Yarlung-Zangpo Suture YZS), and Bangong-Nujiang Suture (BNS). The major blocks are Himalaya Block (HB), Lhasa Block (LB), and Qiangtang Block (QB). The white line is the projection line of the profiles in Fig. 4.4, Fig. 4.5, and Fig. 4.6.

CHAPTER 2: METHODS

Receiver functions

The receiver function is an essential method that has been widely used to study crustal structure beneath receiver arrays (Burdick and Langston, 1977; Langston, 1977; Langston, 1979). The unprocessed seismic data that are required by receiver function should have three components of data, V (vertical component), R (radial component), and T (transverse component). The teleseismic or deep event regional P wave waveforms, *D(t)*, are represented by the following equations:

$$D_V(t) = I(t) * S(t) * E_V(t), \quad (2.1)$$

$$D_R(t) = I(t) * S(t) * E_R(t), \quad (2.2)$$

$$D_T(t) = I(t) * S(t) * E_T(t), \quad (2.3)$$

where I(t) is the impulse response of the recording instrument, S(t) is source time function, E(t) with subscript V, R, and T represents the transfer function of the crust-mantle structure beneath the recording instrument (Langston, 1979).

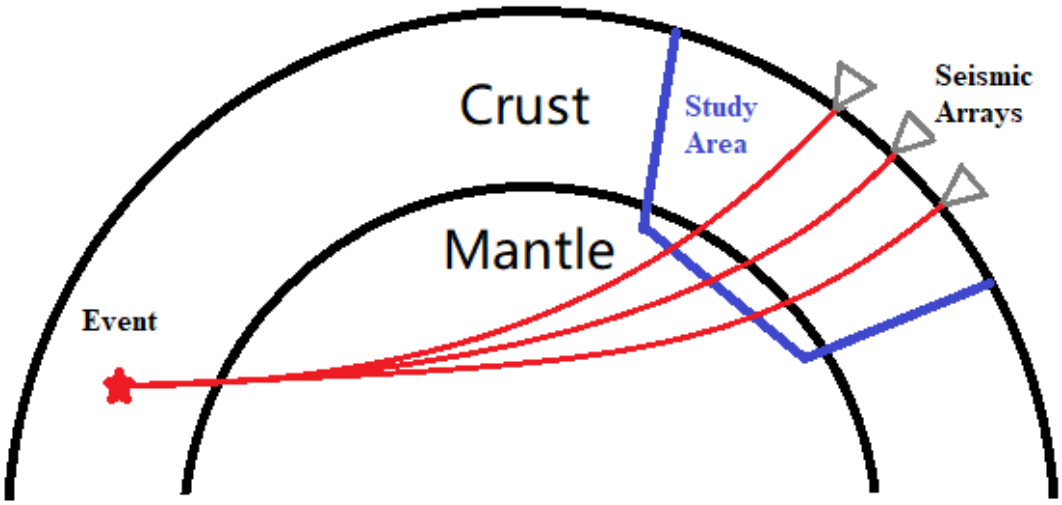

Figure 2.1: Basic scheme of teleseismic tomography. The red star represents the teleseismic source. The red lines are the ray paths. The blue box shows the study area. The grey triangles are the seismic arrays (recording instruments).

Since teleseismic P-wave arrives at instruments in steep incident angles (Fig. 2.1), the vertical component of the instrument responses includes a major direct arrival and a few minor late arrivals from reverberations and phase conversions in the Moho discontinuity (Burdick and Helmberger, 1974; Burdick and Langston, 1977). Thus the transfer function of the crust-mantle structure of vertical component can be neglected, and assume that $D_V(t)$ behaves like a Dirac delta function (Langston, 1979).

$$D_V(t) \cong I(t) * S(t) \tag{2.4}$$

By assuming the instrument responses are matched between components, the transfer functions in radial and transverse components can be expressed in the frequency domain by

$$E_R(\omega) = \frac{D_R(\omega)}{I(\omega)S(\omega)} \cong \frac{D_R(\omega)}{D_V(\omega)} \tag{2.5}$$

$$E_T(\omega) = \frac{D_T(\omega)}{I(\omega)S(\omega)} \cong \frac{D_T(\omega)}{D_V(\omega)} \tag{2.6}$$

$E_R(\omega)$ and $E_T(\omega)$ are transformed back into the time domain by applying Fourier transform and Gaussian function and given the transfer functions as the typical receiver functions (Langston, 1979).

Traditional H-κ method

The traditional H-κ stacking method was developed by Zhu and Kanamori (2000) to calculate the depth of Moho discontinuity and the Vp/Vs ratio beneath a seismic array by stacking the receiver functions of teleseismic P-wave sources. The H represents the depth of Moho discontinuity (thickness of Earth crust), and the κ represents the ratio of P wave and S wave velocities (Vp/Vs). The first calculation of the H and κ are performed by solving the P-to-S conversion dominated radial receiver function. Due to the large velocity contrast at the Moho discontinuity, the Moho P-

to-S conversion (Ps) should be the largest signal followed by the direct P (Fig. 2.4). Ideally, the main phase (Ps) and its multiple phases *PpPs* (M1), and *PsPs* + *PpS*s (M2) should be easy to identify with clear amplitude (Fig. 2.4). Then the theoretical arrival times of the main phase and its multiples are calculated. The stacking of radial receiver function is based on the input values of Standard Southern California Velocity Model (Fig. 2.3). All the receiver functions are stacked based on theoretical arrival times of all phases and the sum of amplitudes is computed as:

$$s(H,\kappa) = \omega_1 r(t_1) + \omega_2 r(t_2) - \omega_3 r(t_3) \tag{2.7}$$

where r(t) represents the radial receiver function, t_1, t_2, and t_3 are the theoretical arrival times of *Ps*, M1, and M2. The ω_i's are weighting factors, and the sum of the factors is 1, where$\omega_1 = 0.7$, $\omega_2 = 0.2$, and ω_3=0.1. The $s(H,\kappa)$ meets at a maximum point where all three phases are stacked concordantly with the correct H and κ (Fig. 2.2 a). The variances of H and κ can be obtained by using the Taylor expansion of $s(H,\kappa)$ at the maximum and neglecting the higher order terms:

$$\sigma_H^2 = 2\sigma_s / \frac{\partial^2 s}{\partial H^2} \tag{2.8}$$

$$\sigma_\kappa^2 = 2\sigma_s / \frac{\partial^2 s}{\partial \kappa^2} \tag{2.9}$$

where s is the estimated variance of $s(H,\kappa)$ from stacking.

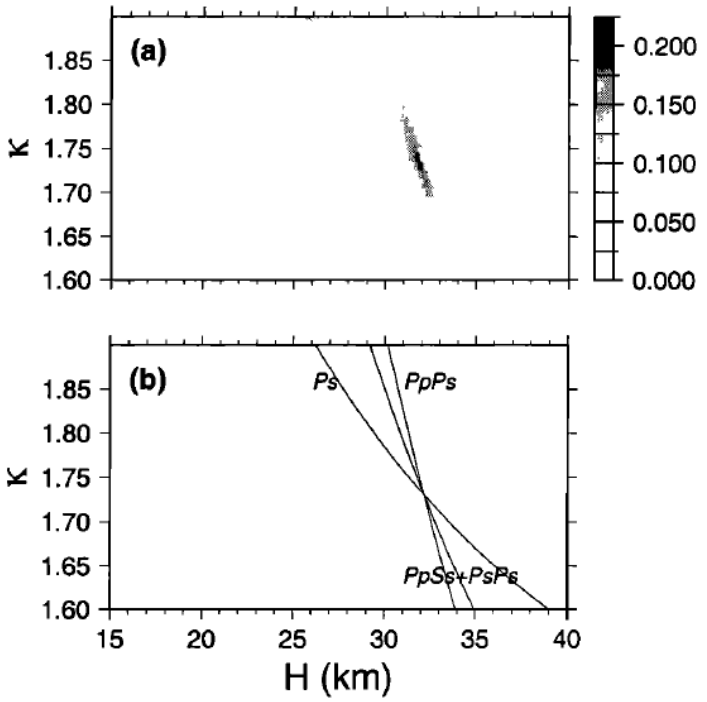

Figure 2.2: (a) The s(H, κ) from stacking the receiver functions in Fig. 2.4. The dark spots represents the maximum when the correct crustal thickness and Vp/Vs ratio are use in the stacking. (b) H-κ relations for Ps, PpPs (M1), and PpSs+PsPs (M2) phases in Fig. 2.4. Each curve represents the contribution from its converted phase to the stacking. (from Zhu and Kanamori, 2000))

Layer	Thickness, km	V_s, km/s	V_p/V_s
1	5.5	3.18	1.730
2	10.5	3.64	1.731
3	16.0	3.87	1.731
4	—	4.50	1.733

Figure 2.3: The Standard Southern California Velocity Model (Table 1, from Zhu and Kanamori, 2000)) (Wald et al., 1995)

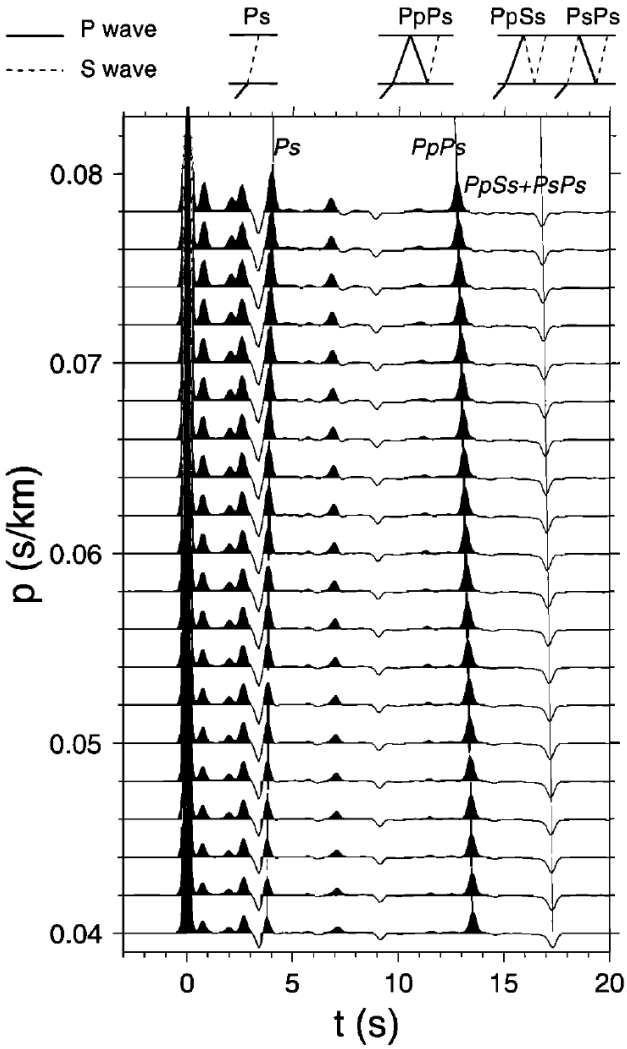

Figure 2.4: Radial receiver function as a function of ray parameter p based on the Standard Southern California Velocity Model (Fig. 2.3). The Moho converted phase Ps, and its multiples PpPs, PpSs+PsPs are labeled on the top. (from Zhu and Kanamori, 2000)

Generalized H-κ method

The H-κ method (Zhu and Kanamori, 2000) has been widely used to estimate the crustal thickness (H) and the ratio of P to S velocities (Vp/Vs ratio, κ) with receiver functions. The radial receiver functions (R-RF) stacking results in Figure 2.4 are not agreed with the input values in Figure 2.3 since the method presume the isotropic crust and flat Moho. Therefore, in regions where the crustal structures and tectonic settings are complicated, the method may produce uncertain or even

unrealistic results, particularly from regions with dipping Moho and crustal anisotropy. Recently, Li et al. (2108, submitted) proposed a generalized H-κ method with harmonic correction (cHκ), which include corrections for these effects before stacking. General cases with moderate plunging anisotropy and dipping interfaces for multiple layers can be fitted by using cosθ (two-lobed) and cos2θ (four-lobed) functions to correct both Ps and its crustal multiples M1 and M2:

$$F(\theta) = A_0 + A_1 \cos(\theta - \theta_1) + A_2 \cos 2(\theta - \theta_2) \tag{2.10}$$

where A_0 is central arrival time, A_1, and A_2 are amplitudes of the cosθ and cos2θ variations, and θ_1 and θ_2 are phases of variations (Fig. 2.5) (Li et al., 2018, submitted). Based on Raysum (Frederiksen and Bostock, 2000), synthetic tests of models with various plunging anisotropy, dipping angles, and dipping directions show that Ps, M1, and M2 can be well fitted by cosθ and cos2θ functions. To avoid overweighting in certain azimuthal angle and enhance the signal-to-noise ratio of each R-RF, the corrected receiver functions are stacked into azimuthal bins of 5° (Kaviani and Rümpker, 2015) (Fig. 2.5). Correcting for the azimuthal variations significantly enhanced the H-κ stacking. To calculate the best solution of the five parameters in Equation 2.10, the grid search of harmonic fitting using:

$$\begin{aligned} &SUM(\tau_D, \varphi_D, \tau_A, \varphi_A, \mathrm{m}) \\ &= \left| \frac{1}{M} \sum_{\theta}^{M} \left[R'_G(t_{Ps}) \cdot \left| R'_G(t_{Ps}) \right|^{-\frac{3}{4}} \right] \right|^3 \cdot \frac{1}{M} \sum_{\theta}^{M} \left[R'_G(t_{Ps}) \cdot \left| R'_G(t_{Ps}) \right|^{-\frac{3}{4}} \right] \end{aligned} \tag{2.11}$$

where M is the number of stacked azimuthal bins, R'_G is the binned R-RFs after 5° stacking (Li et al., 2018, submitted). The search ranges for the parameters are A_0 from -1.0 to 1.0 s; A_1 and A_2 from 0 to 0.75 s; θ_1 from 2.5 to 357.5°; θ_2, 2.5 to 177.5°. With more reliable M1 than the traditional method, the weighting factors of Equation 2.7 are changed to $\omega_1 = 0.5$, $\omega_2 = 0.4$, and ω_3=0.1 (Fig. 2.5 e). With The results show apparent improvement compared to the traditional H-κ method,

with clearer traces of multiples and stronger stacking energy in the grid search, as well as more reliable H-κ values with small variances.

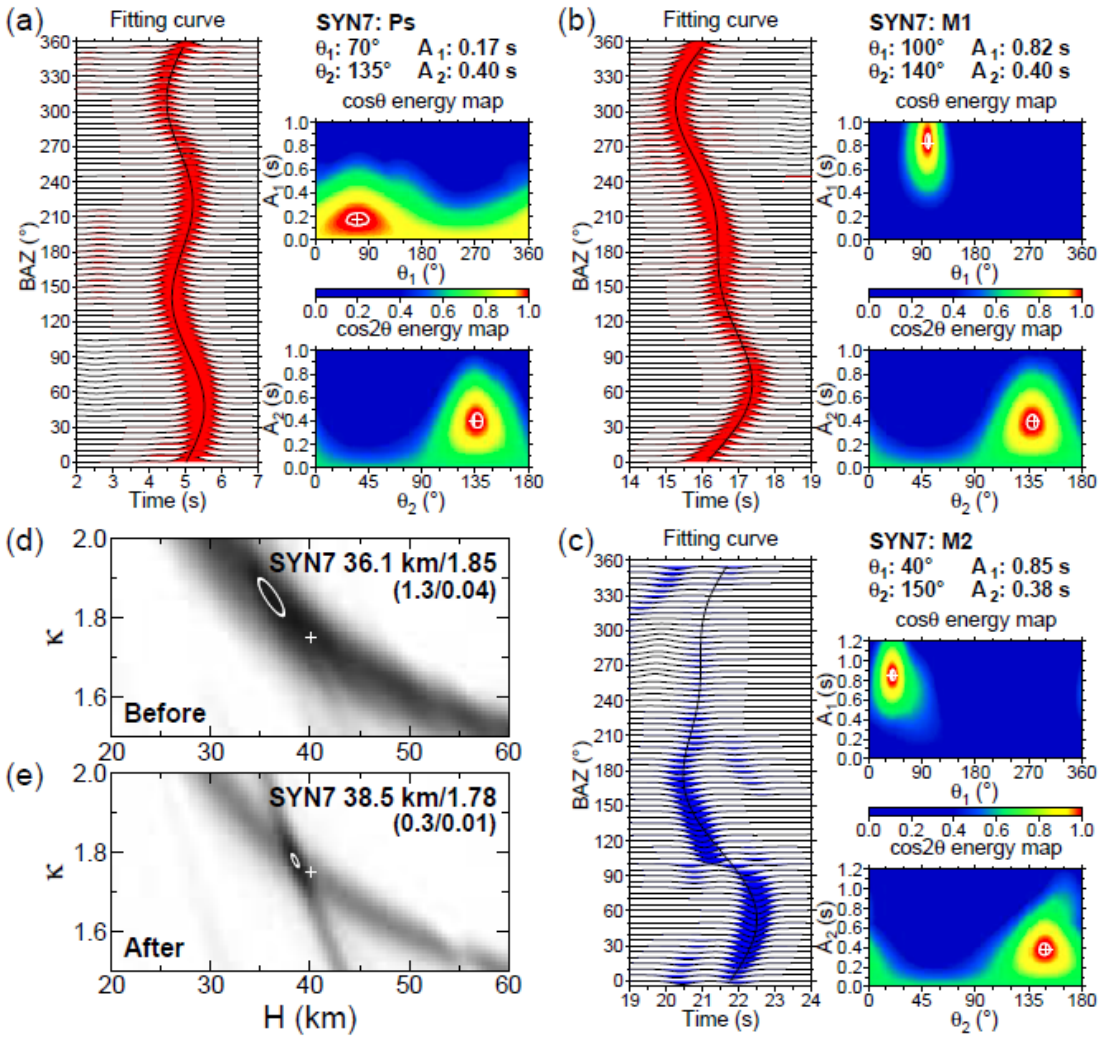

Figure 2.5: Harmonic fitting of the arrival times of Ps (a), M1 (b), and M2 (c) in R-RFs. (d) is H-κ stacking result before the harmonic correction for the complex model, and (e) is the result after the harmonic correction for the complex model (SYN7). The fitting curve with both cosθ and cos2θ functions, energy stacking maps of the grid search for harmonic parameters, and the search results are shown in (a-c). The weighting of phases Ps, M1, and M2 in traditional H-κ method is 0.7, 0.2, 0.1 in (d), and the weighting is 0.5, 0.4, 0.1 in (e). (Li et al., submitted)

CHAPTER 3:STUDY REGION AND DATA

Hi-CLIMB Seismic Array

Over past thirty years, several regional-scale seismic arrays have been deployed in Tibetan Plateau to study the crustal and upper mantle structures and understand the process and mechanism of Indian-Eurasian continental collision. such as PASSCAL (Owens et al., 1993), Namcha Barwa (Sol et al., 2007), INDEPTH II (Brown et al., 1996; Nelson et al., 1996), III (Huang et al., 2000), IV (Zhao et al., 2001; Zhao et al., 2008), BHUTAN (Velasco et al., 2007), HIMNT (de la Torre and Sheehan, 2005), RISE (Jin et al., 2009). Many studies, which used data provided these arrays, provided stunning results of crustal and upper mantle structures with different methods. Although these studies revealed the subduction of the Indian Plate beneath the uplifting Tibetan Plateau and partial melt flow, most of these studies were focused on the eastern Tibetan Plateau and central-eastern Tibetan Plateau.

In 2002, the Hi-CLIMB (Himalaya-Tibetan Continental Lithosphere during Mountain Building) project was launched in the central western Tibetan Plateau. The major part of the project was made up of approximately 150 temporary stations (Table A.1, H0010 to H1630), which were functional from September 2002 to August 2005. The close-spaced stations of the dense linear array covered from Ganges Basin (GB), northward across Main Boundary Thrust (MBT), Himalayas Block (HB), the Yarlung-Zangpo Suture (YZS), Lhasa Block (LB), Bangong-Nujiang Suture (BNS), and Qiangtang Block (QB) (Fig. 1.1) (Nabelek et al., 2009, project summary). Two adjacent stations were deployed approximately five kilometers apart.

Teleseismic Data

Teleseismic P-wave data from the 2002-2005 Hi-CLIMB array were collected and processed by Professor Lupei's group. As shown in Figure 1.1, the 150 stations are distributed approximately as a linear line along 85°E and covered from 27°N to 34°N. A 0.05-2.0 Hz band-pass filter to all seismograms. All the earthquake events have magnitude 5 or larger on Richter scale. 2082 teleseismic events with clear P-wave signals were used to compute receiver functions. A total number of 52,692 receiver functions are used in the generalized H-κ method to compare the results before and after the corrections.

CHAPTER 4: RESULTS

H-κ stacking results

The H-κ stacking with harmonic corrections (cHκ) was applied to all the stations of Hi-CLIMB seismic array. Due to the uncertain effects on sediments and large noise signal due to the river channels, we exclude the stations H0010 to H0250 located in the GB (Fig. 4.1). To better constrain the searching range for H and κ maximum point (Fig. 2.2 a), the ranges for H are separated into two groups at 28.5°N based on results from Xu and Song (2013), 35 km to 60 km for stations from H260 to H540, and 55 km to 80 km for the rest of the stations. The reasonable κ results should be from 1.6 to 2.0. After detailed examination and selection, only stations (103 out of 122 stations) with broad azimuthal coverage, clear *Ps*, and M1 phases, and strong H-κ maximum points are kept (Fig. 4.1, blue triangles). Here are two best examples from the stacking, H0310 in the HB (Fig. 4.2) and H1630 in the QB (Fig. 4.3). More examples are provided in the supplementary figures (Fig. B.1-B.8). As shown in the examples below, the amplitudes of Ps and M1 phases are clear and reliable. The energy maps of grid search also support the accuracy of the calculation of the arrival times. The maximum points in the H-κ stacking of the after-corrected ones (Fig. 4.2 e; Fig. 4.3 e) are much clearer than the ones in the before-corrected ones (Fig. 4.2 d; Fig. 4.3 d). Also, the variances of H and κ in Figure 4.2 e and 4.3 e are much smaller than the ones in Figure 4.2 d and 4.3 d.

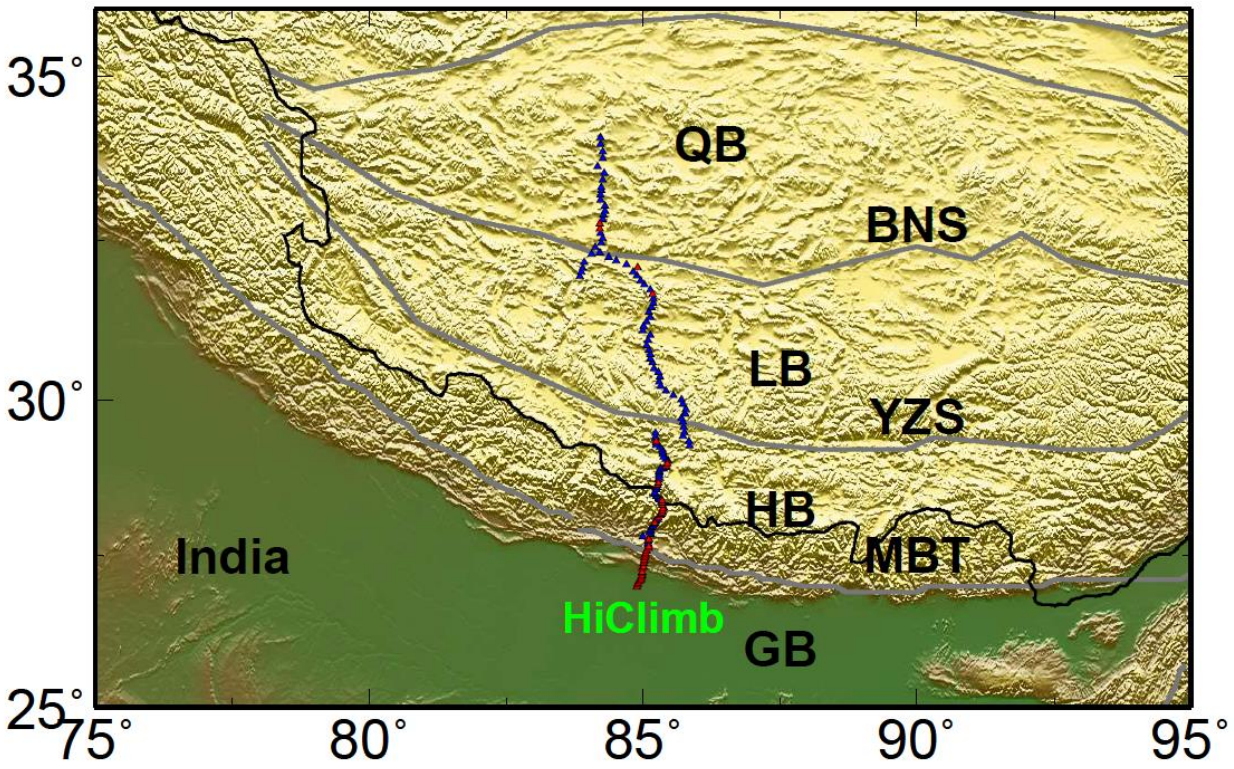

Figure 4.1: Include the same tectonic blocks in Tibetan Plateau and locations of Hi-CLIMB seismic array as Fig.1.1. The blue triangles show the 103 stations whose data is used in the study. The red triangles show the rest of stations whose data is not used.

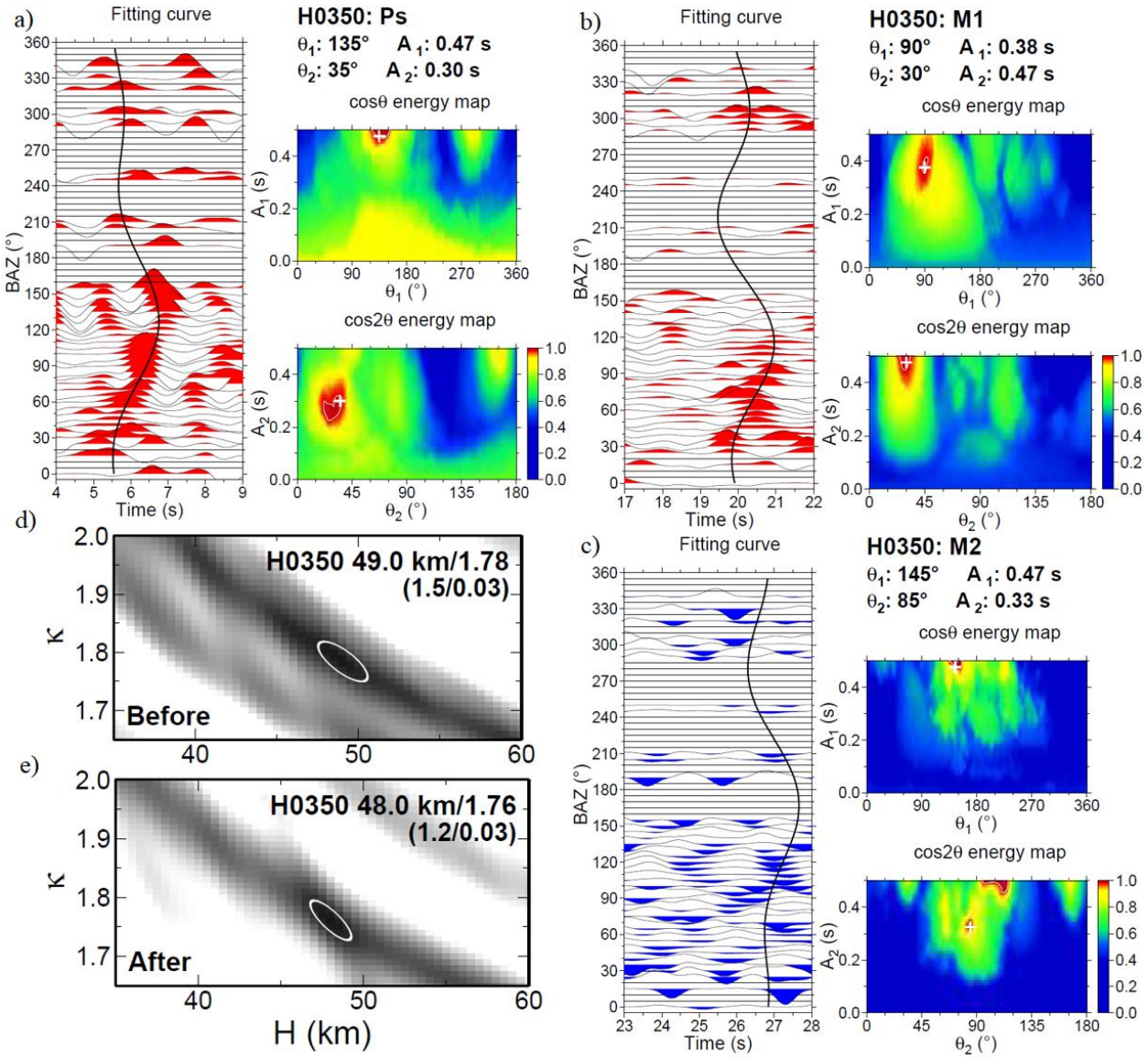

Figure 4.2: Harmonic fitting of the arrival times of Ps (a), M1 (b), and M2 (c) in R-RFs of station H0350. (d) is H-κ stacking result before the harmonic correction, and (e) is the result after the harmonic correction. The fitting curve with cosθ and cos2θ functions, energy stacking maps of the grid search for harmonic parameters, and the search results are shown in (a-c). The weighting of phases Ps, M1, and M2 in traditional H-κ method is 0.7, 0.2, 0.1 in (d), and the weighting is 0.5, 0.4, 0.1 in (e).

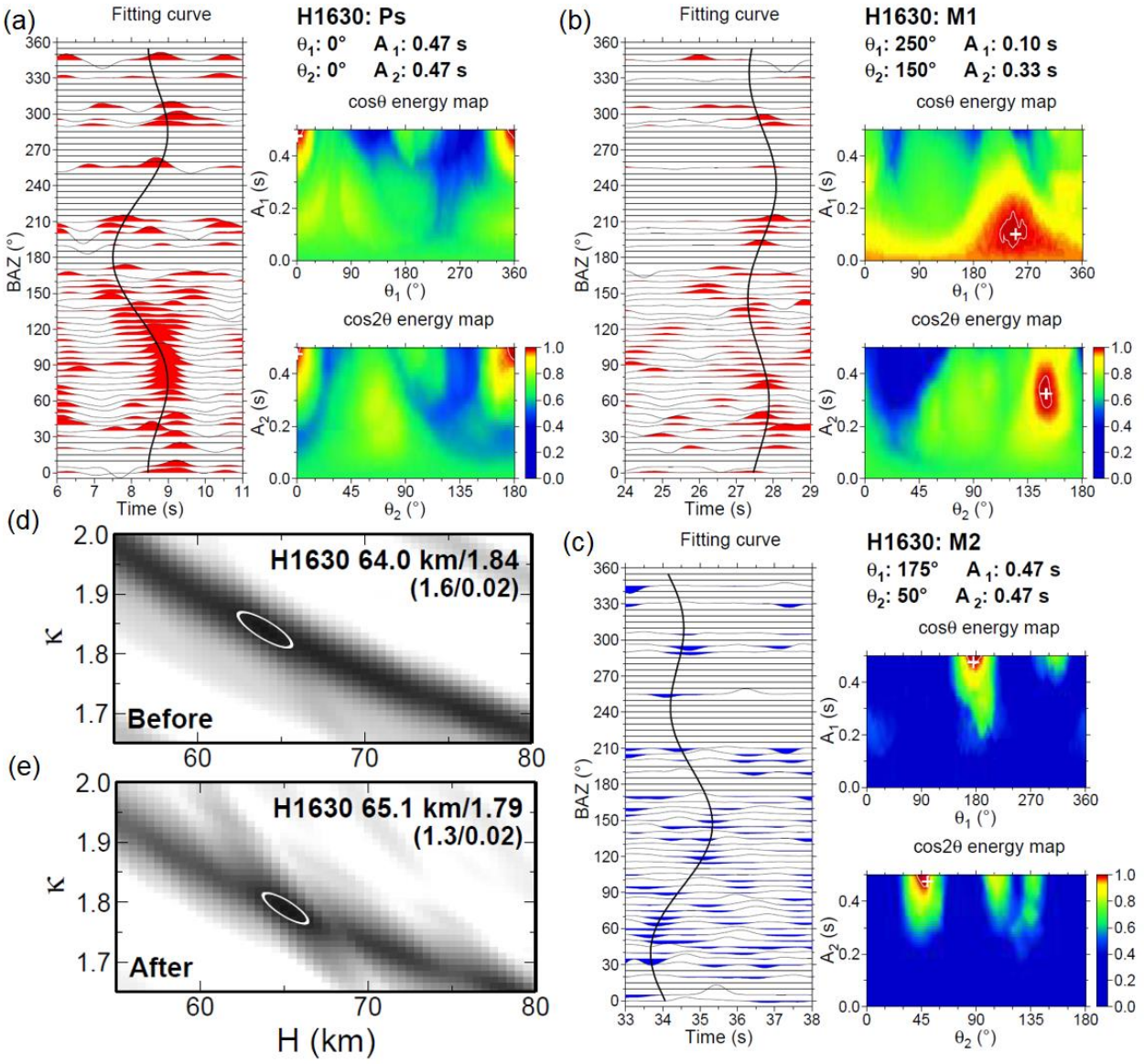

Figure 4.3: Harmonic fitting of the arrival times of Ps (a), M1 (b), and M2 (c) in R-RFs of station H1630. (d) is H-κ stacking result before the harmonic correction, and (e) is the result after the harmonic correction. The fitting curve with cosθ and cos2θ functions, energy stacking maps of the grid search for harmonic parameters, and the search results are shown in (a-c). The weighting of phases Ps, M1, and M2 in traditional H-κ method is 0.7, 0.2, 0.1 in (d), and the weighting is 0.5, 0.4, 0.1 in (e).

Vp/Vs Result

The dispersed data (Fig. 4.4; Fig. 4.5) shows that the Vp/Vs ratios of stations near YZS, LB, and southern QB is much larger than the ones of stations on the lower Himalaya, and northern QB. In order to compare the Vp/Vs results before and after the corrections, the average value of all data in a 0.5-degree range is calculated, and the next range is shifted northward by 0.1 degree. The 61 average points are connected by the red line to show the pattern across the array. The standard deviation of the data in each 0.5-degree range is also calculated to show the dispersion of the data. As shown in Figure 4.4 and 4.5, the result of the generalized method after correction shares a similar pattern with the one without the corrections. However, the dispersion and standard deviation of the data in Figure 4.5 is much smaller than the dispersion in Figure 4.4.

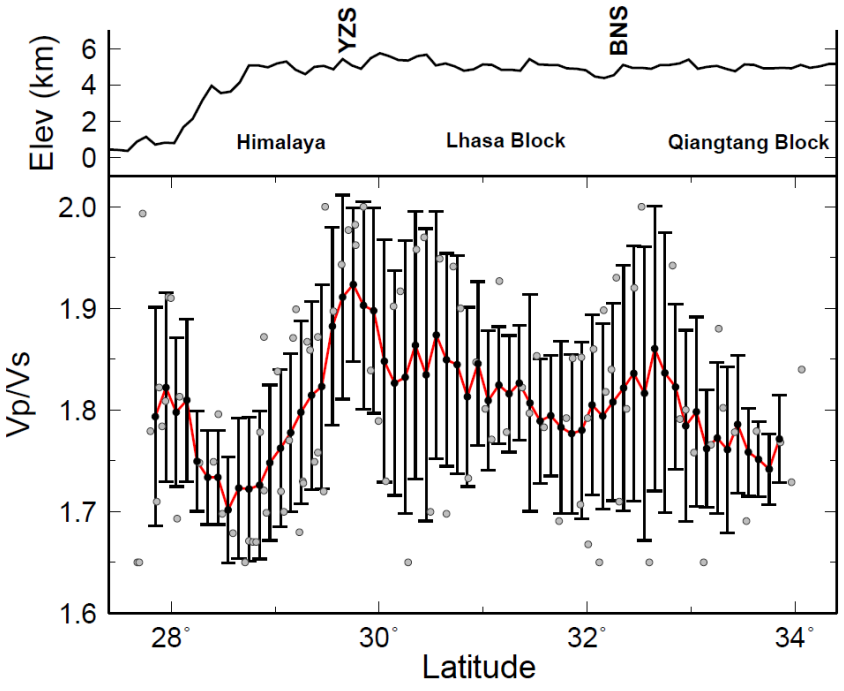

Figure 4.4: Profiles of Vp/Vs ratio along the 85°E line marked as the white line in Figure 1.1. The grey dots show κ values beneath every station before the correction. The black dots are the mean value of all the κ values in 0.5-degree range. The range is moved by every 0.1 degree from 27.6°N to 34.1°N. The black error bars represent the standard deviation of all the κ values in 0.5-degree range.

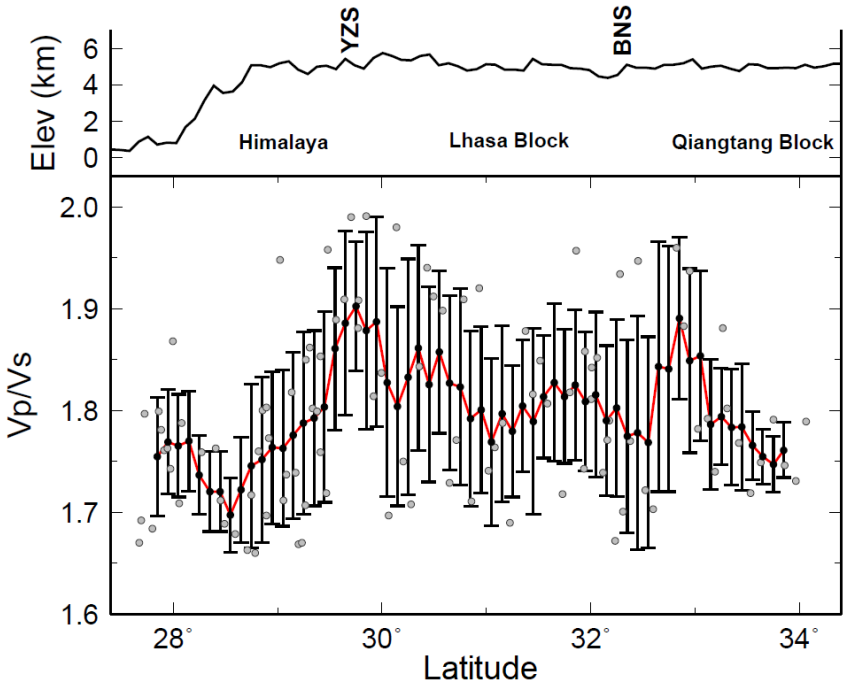

Figure 4.5: Profiles of Vp/Vs ratio along the 85°E line marked as the white line in Figure 1.1. The grey dots show κ values beneath every station after the correction. The black dots are the mean value of all the κ values in 0.5-degree range. The range is moved by every 0.1 degree from 27.6°N to 34.1°N. The black error bars represent the standard deviation of all the κ values in 0.5-degree range.

Moho depth result

The Moho depth (H) results indicate the crust is northward thickening from 50 km to 80 km (Fig. 4.6). Since we exclude the stations located in the GB due to the uncertain in the stacking by the sediment thickness, the Moho depth (H) cover from the HB to QB. The H values are about constant from 27.5°N to 28.5°N in the lower Himalaya and are increased linearly from 50 km at 28.5°N to 78 km at 29.3°N. The H results in HB agree with the topography change and Isostasy. We also observe strong duplex Moho discontinuity at approximately 60 km and 75 km from 29.4°N to 31°N beneath the LB. However, most of the stations indicate shallower Moho depths. From 31.5°N to 32.5°N, the Moho depths continuously stay around 75 km until BNS. However, the H results from a few stations near BNS, northern LB, southern QB shows the Moho depth is around 55 km.

The Moho depths become shallower at around 65 km in the QB. Comparing to the results of traditional H- κ method, over 90% of the corrections in our results are less than 10 km (Fig. 4.7).

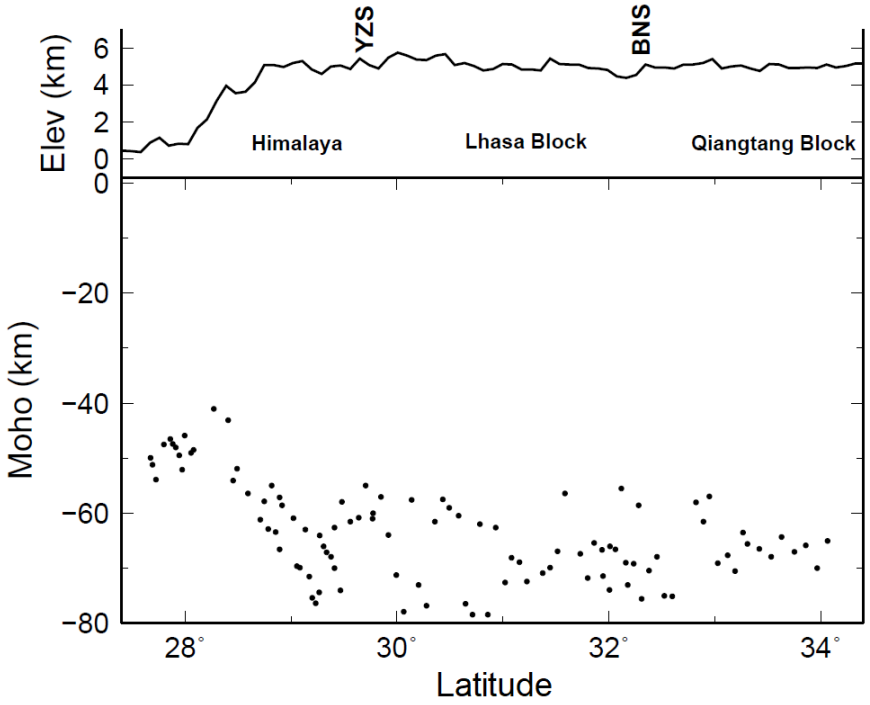

Figure 4.6: Profiles of Moho depth along the 85°E line marked as the white line in Figure 1.1. The black dots are the Moho depths beneath every station.

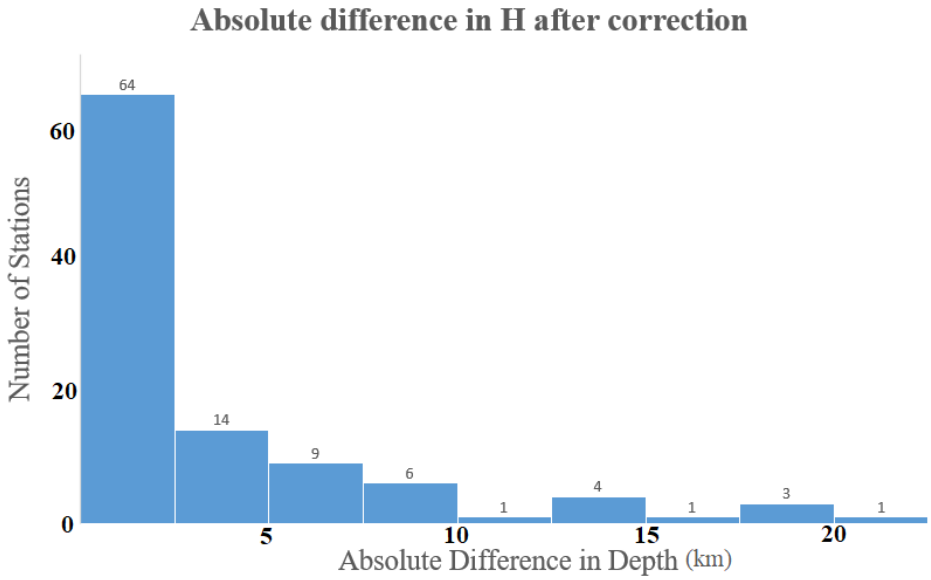

Figure 4.7: The histogram shows all the absolute differences in Moho depth between before and after correction. The bin width of each column is 2.5 km.

CHAPTER 5:DISCUSSION

The Vp/Vs ratio results of station southern LB and southern QB have larger values than the rest of the areas. The shear velocity structure from Xu and Song (2013) shows two mid-crust low velocity zones in similar locations as our result. Similar results were reported along with other seismic arrays by receiver function study of Kind et al. (1996), and surface wave tomography study of Sun et al. (2010). The large Vp/Vs ratio may suggest potential partial melting in these regions. Hung et al. (2010) also show that a gentle northward dipping of the Indian mantle north of BNS and hardly any evidence of down-welling between 100 km and 400 km in the mantle. Therefore, the high Vp/Vs zone can be interpreted as a result of strong deformation.

Another minor increase of Vp/Vs ratio in central and northern LB is also observed in the shear velocity structure from Xu and Song (2013). The lower Vp/Vs ratio is suggested to be an eclogite layer under the LB (Wittlinger et al., 2004). Such a discontinuous pattern, which agrees with the results of Hung et al. (2010) and Xu and Song (2013), suggests that the channel flow model may be reconsidered. However, such mid-crust low velocity zones and high Vp/Vs ratio zones are not observed in the receiver function study of Nabelek et al. (2009).

The sharp dipping of crust from 28.5°N to 29.3°N suggests the existence of a high velocity zone beneath the HB, which agrees with the shear velocity structure from Xu and Song (2013). The duplex Moho discontinuity at approximately 60 km and 75 km from 29.4°N to 31°N beneath the LB (Fig. 4.6) strongly agrees with the result of Nabelek et al. (2009). The strong conversions at both top and bottom of lower crust beneath LB belong to the under-plating Indian plate (Nabelek et al., 2009]. Such duplex Moho discontinuity was also observed in western and eastern part of LB (Owens et al., 1993; Kind et al., 2002; Wittlinger et al., 2004). The duplex crustal structure also

agrees with our Vp/Vs ratio result. The upper layer of the crust can be interpreted as a partially melting Indian crust.

The crustal structures from northern LB to southern QB were suggested to be very complex by the Gaussian beam migration study of Nowack et al. (2010). The crustal layer with gradual change from 55 km to 65 km of lower H values from northern LB to southern QB can be interpreted to belong to the QB or the Eurasian Plate. The lower H values beneath BNS also fits the second high of the Vp/Vs zone, which is also interpreted as the partial melting of Eurasian crust. Since crustal layer with H values at around 70 km depth are consistent with the average values at the duplex, this layer can be interpreted as the northern end (around 31.5°N) of the subducting Indian Plate, which agrees with the results of Nabelek et al. (2009).

CHAPTER 6: CONCLUSION

We have successfully applied the generalized H-κ method (cHκ) to calculate the Moho depth and Vp/Vs ratio using radial receiver function data of Hi-CLIMB seismic array. With harmonic correction, the H and κ results of our study agree with many past studies in many points of view. The generalized H-κ method (cHκ) generated a clear Moho image and well-fitted Vp/Vs ratio profile along Hi-CLIMB seismic array. The duplex Moho discontinuity at approximately 60 km and 75 km from 29.4°N to 31°N beneath the Lhasa Block, and the overriding Eurasian plate at 55 km to 60 km from 31.5°N to 33.5°N are correlated with the high Vp/Vs ratio in southern Lhasa Block and southern Qiangtang Block. These two zones are interpreted as the partial melting of the crust of Indian Plate and Eurasian Plate. The sharp curve of the Vp/Vs ratio results that agrees with the shear velocity of Xu and Song (2013) indicate discontinued pattern instead of the channel flow model of Clark and Royden (2000). The linear depth profile along 85°E suggested that the crust thickens from about 50 km beneath lower Himalaya to over 75 km beneath Lhasa Block and finally becomes shallower at around 65 km beneath Qiangtang Block. The northern extent of Indian crust is observed to be between the Yarlung-Zangpo Suture and Bangong-Nujiang Suture at around 31.5°N. An accurate H value can help geologist better understand the collision between Indian and Eurasian plates, and mechanism behind it, as well as an accurate κ value can offer better constraints to study mineral composition and melting condition of the crust.

REFERENCES

Argand, E., 1922. La tectonique de l'Asie. *13th Congrès Géologique International Belgique, Rep. 1*, 171-372

Brown, L.D., Zhao, W.J., Nelson, D.K., Hauck, M., Alsdorf, D., Ross, A., Cogan, M., Clark, M., Liu, X.W., Che, J.K., 1996. Bright spots, structure, and magmatism in southern Tibet from INDEPTH seismic reflection profiling. *Science 274*, 1688–1690.

Burdick, L. J., and Helmberger, D. V., 1974. Time functions appropriate for deep earthquakes, *Bull. Seismol. Soc. Amer., 64*, 1419-1428.

Burdick, L. J., and Langston, C. A., 1977. Modeling crustal structure through the use of converted phases in teleseismic body-wave forms, *Bull. Seismol. Soc. Amer., 67*, 677-691.

Clark, M.K., Royden, L.H., 2000. Topographic ooze: building the eastern margin of Tibet by lower crustal flow. *Geology 28*, 703–706.

de la Torre, T., Sheehan, A., 2005. Broadband seismic noise analysis of the Himalayan Nepal Tibet seismic experiment. *Bull. Seismol. Soc. Am 95*, 1202–1208.

Dewey, J. F., Shackleton, R. M., Chang, C., and Sun, Y., 1988. The tectonic evolution of the Tibetan Plateau. *Phil. Trans. R. Soc. Lond, 327*, 379-413.

Frederiksen, A. W., & Bostock, M. G., 2000. Modelling teleseismic waves in dipping anisotropic structures. *Geophysical Journal International, 141(2)*, 401-412.

Huang, W.C., Ni, J.F., Tilmann, F., Nelson, D., Guo, J.R., Zhao, W.J., Mechie, J., Kind, R., Saul, J., Rapine, R., Hearn, T.M., 2000. Seismic polarization anisotropy beneath the central Tibetan Plateau. *J. Geophys. Res. 105*, 27979–27989.

Hung, S.-H., Chen, W.-P., Chiao, L.-Y., Tseng, T.-L., 2010. First multi-scale, finite frequency tomography illuminates 3-D anatomy of the Tibetan Plateau. *Geophysical Research Letters 37*, L06304.

Jin, G., Chen, Y., Basang, C., 2009. Investigation of local earthquakes in the Lhasa region. *Chin. J. Geophys 52*, 3020–3026.

Kaviani, A., & Rümpker, G., 2015. Generalization of the H-κ stacking method to anisotropic media. *Journal of Geophysical Research: Solid Earth, 120(7),* 5135-5153.

Kikuchi, M., and H. Kanamori, 1982. Inversion of complex body waves. *Bull. Seismol. Soc. Am., 72*, 491-506.

Kind, R., et al., 2002. Seismic images of crust and upper mantle beneath Tibet: evidence for Eurasia plate subduction. *Science 298*, 1219–1221.

Langston, C. A., 1979. The effect of planar dipping structure on source and receiver responses for constant ray parameter. *Bull. Seismol. Soc. Am., 67*, 1029-1050.

Ligorria, J. P., and Ammon, C. J., 1999. Iterative deconvolution and receiver-function estimation. *Bull. Seismol. Soc. Am., 85*, 1395-1400.

Mitra, S., K. Priestley, A. K. Bhattacharyya, and Gaur, V. K., 2005. Crustal structure and earthquake focal depths beneath northeastern India and southern Tibet. *Geophys. J. Int., 160*, 227-248.

Nabelek, J., Hetenyi, G., Vergne, J., et al., 2009. Underplating in the Himalaya–Tibet collision zone revealed by the Hi-CLIMB experiment. Science 325, 1371–1374.

Nelson, K., Zhao, W., Brown, L., Kuo, J., Che, J., Liu, X., et al., 1996. Partially molten middle crust beneath southern Tibet: Synthesis of project INDEPTH results. *Science, 274(5293),* 1684-1688.

Owens, T.J., Zandt, G., 1997. Implications of crustal property variations for models of Tibetan Plateau evolution. *Nature 387,* 37–43.

Patriat, P., and Achache, J., 1984. India-Eurasia collision chronology has implications for crustal shortening and driving mechanism of plates. *Nature, 311,* 615-621.

Royden, L. H., Burchfiel, B. C., & van der Hilst R. D., 2008. The Geological Evolution of the Tibetan Plateau. *Science, 321*, 1054-1058.

Sol, S., Meltzer, A., Burgmann, R., Hilst, R.D, v.d., King, R., Chen, Z., Koons, P.O., Lev, E., Liu, Y.P., Zeitler, P.K., Zhang, X., Zhang, J., Zurek, B., 2007. Geodynamics of the southern Tibetan Plateau from seismic anisotropy and geodesy. *Geology 35*, 563–566.

Sun, X.L., Song, X.D., Zheng, S.H., et al., 2010. Three dimensional shear wave velocity structure of the crust and upper mantle beneath China from ambient noise surface wave tomography. *Earthquake Science 23*, 449–463.

Tapponnier, P., Z. Xu, F. Roger, B. Meyer, N. Arnaud, G. Wittlinger, and Y. Jingsui, 2001: Oblique stepwise rise and growth of the Tibet Plateau. *Science, 294*, 1671-1677.

Tseng, T., Chen, W., and Nowack, R. L., 2009. Northward thinning of Tibetan crust revealed by virtual seismic profiles, *Geophys. Res. Lett., 36, L24,304-L24,309*.

Velasco, A.A., Gee, V.L., Rowe, C., Grujic, D., Hollister, L.S., Hernandez, D., Miller, K.C., Tobgay, T., Fort, M., Harder, S., 2007. Using small, temporary seismic networks for investigating tectonic deformation: brittle deformation and evidence from strike-slip faulting in Bhutan. *Seismol. Res. Lett. 78*, 446–453.

Wittlinger, G., Farra, V., Vergne, J., 2004. Lithospheric and upper mantle stratifications beneath Tibet: New insights from Sp conversions. *Geophysical Research Letters, 31(19)*.

Xu, Z. J., Song, X., & Zhu, L., 2013. Crustal and uppermost mantle S velocity structure under Hi-CLIMB seismic array in central Tibetan Plateau from joint inversion of surface wave dispersion and receiver function data. *Tectonophysics*, *584*, 209-220.

Zhang, Z., Deng, Y., Teng, J., Wang, C., Gao, R., Chen, Y., & Fan, W., 2011. An overview of the crustal structure of the Tibetan plateau after 35 years of deep seismic soundings. *Journal of Asian Earth Sciences, 40(4)*, 977-989.

Zhao, W., et al., 2001. Crustal structure of central Tibet as derived from project INDEPTH wide-angle seismic data, *Geophys. J. Int., 145*, 486-498.

Zhao, W., Brown, L., Wu, Z., Klemperer, S.L., Shi, D., Mechie, J., Su, H., Tilmann, F., Karplus, M.S., Makovsky, Y., 2008. Seismology across the northeastern edge of the Tibetan Plateau. EOS Trans. *AGU 89*, 487.

APPENDIX A: HI-CLIMB STATIONS

Table A.1 List of station names, latitudes, longitudes, elevations of Hi-CLIMB seismic array. All data is required from IRIS Data Center

Station Name	Latitude (° N)	Longitude (° E)	Elevation (m)
H0010	26.9833	84.8932	22
H0020	27.0176	84.905	24
H0030	27.0408	84.9074	27
H0040	27.0665	84.9373	33
H0050	27.0871	84.9533	38
H0060	27.1079	84.9671	42
H0070	27.1344	84.9699	51
H0080	27.1661	84.984	75
H0090	27.2018	84.9793	113
H0100	27.2305	84.9872	162
H0120	27.2829	84.9885	267
H0130	27.3152	85.0081	523
H0150	27.3698	85.0137	647
H0160	27.3953	85.0221	461
H0170	27.4196	85.0251	396
H0180	27.4514	85.0328	475
H0190	27.4717	85.0422	505
H0200	27.499	85.045	563
H0210	27.5287	85.047	809
H0220	27.5583	85.0697	1883
H0230	27.58	85.0733	2316
H0240	27.6078	85.107	2153
H0250	27.6312	85.1009	1737

Table A.1 Hi-CLIMB seismic array station information (continued).

H0260	27.6733	85.0928	1854
H0270	27.6957	85.0902	1597
H0280	27.727	85.0961	1289
H0290	27.7565	85.1119	1162
H0310	27.8005	85.0049	512
H0320	27.8367	85.151	937
H0330	27.8613	85.1168	494
H0340	27.8864	85.1507	545
H0350	27.9112	85.1396	525
H0360	27.9445	85.1645	618
H0370	27.9725	85.1863	595
H0380	27.995	85.2069	1448
H0390	28.0251	85.2217	1965
H0400	28.0572	85.2267	1932
H0410	28.0798	85.2568	1989
H0420	28.107	85.2883	2005
H0430	28.1379	85.3206	1837
H0440	28.1661	85.3416	1442
H0450	28.1946	85.3505	1488
H0460	28.2151	85.3574	1693
H0470	28.2515	85.3676	1757
H0480	28.2708	85.3793	1789
H0490	28.3059	85.3466	1912
H0500	28.3411	85.3524	2243
H0510	28.3863	85.3487	2698
H0520	28.4085	85.3128	2868

Table A.1 Hi-CLIMB seismic array station information (continued).

H0530	28.4537	85.2448	3035
H0540	28.492	85.2224	3199
H0550	28.5168	85.2161	3334
H0560	28.562	85.2464	3612
H0570	28.5948	85.2598	3714
H0580	28.6318	85.2697	3739
H0590	28.6691	85.2808	3810
H0600	28.7112	85.2803	3887
H0610	28.7484	85.3037	3985
H0620	28.7859	85.2959	3989
H0630	28.8196	85.2939	4042
H0640	28.843	85.2945	4028
H0641	28.8562	85.2939	4106
H0650	28.8955	85.3274	4288
H0655	28.8953	85.3824	5113
H0660	28.9169	85.4189	4829
H0670	28.9431	85.4383	4728
H0680	28.9838	85.441	4662
H0690	29.0234	85.455	4701
H0700	29.0559	85.4215	4706
H0710	29.0859	85.3756	4731
H0720	29.1367	85.3643	4685
H0730	29.172	85.3647	4708
H0740	29.2015	85.3564	4620
H0750	29.2348	85.3141	4659
H0760	29.2713	85.2431	4626

Table A.1 Hi-CLIMB seismic array station information (continued).

H0770	29.307	85.2432	4470
H0780	29.3414	85.2372	4678
H0790	29.3803	85.2271	4764
H0800	29.412	85.2313	4785
H0810	29.467	85.2323	4891
H1000	29.2673	85.8577	4560
H1010	29.3355	85.8364	4753
H1020	29.413	85.7369	5039
H1030	29.483	85.7547	5012
H1040	29.5614	85.7398	5115
H1050	29.6387	85.7245	5219
H1060	29.7066	85.7082	5232
H1070	29.7767	85.7634	5261
H1071	29.7702	85.775	5340
H1080	29.8502	85.7827	5403
H1090	29.9222	85.7329	5260
H1100	29.9936	85.6974	5315
H1110	30.0664	85.5526	5435
H1120	30.1381	85.4146	5479
H1130	30.2058	85.3283	5078
H1140	30.2802	85.2968	5185
H1150	30.358	85.3131	5120
H1160	30.434	85.2886	5217
H1170	30.4955	85.1974	4846
H1180	30.5813	85.176	4974
H1190	30.6494	85.1376	4831

Table A.1 Hi-CLIMB seismic array station information (continued).

H1200	30.7152	85.1411	4828
H1210	30.7821	85.1094	4874
H1220	30.8599	85.0688	4776
H1230	30.9321	85.099	4778
H1240	31.0198	85.1341	4731
H1250	31.0842	84.9979	4850
H1260	31.1549	85.0121	4992
H1270	31.2252	85.0721	4726
H1280	31.3016	85.1299	4732
H1290	31.3783	85.103	4822
H1300	31.4454	85.1601	5050
H1310	31.5153	85.1828	5218
H1320	31.5837	85.1894	5225
H1330	31.6558	85.1704	5132
H1340	31.7319	85.1404	5064
H1350	31.8029	85.0323	4973
H1360	31.8623	84.9536	4988
H1370	31.9453	84.8929	4736
H1380	32.0039	84.8227	4638
H1390	32.0724	84.9052	4586
H1400	32.1187	84.6944	4488
H1405	32.1805	84.5131	4636
H1410	32.2361	84.3739	4561
H1415	32.3079	84.2189	4616
H1420	31.9347	83.8425	4955
H1421	32.0088	83.8713	4792

Table A.1 Hi-CLIMB seismic array station information (continued).

H1422	32.0638	83.8993	4620
H1423	32.1587	83.9242	4854
H1425	32.2816	84.0637	4489
H1430	32.3816	84.1311	4485
H1440	32.4545	84.2396	4554
H1450	32.5241	84.2716	4652
H1460	32.5981	84.2235	4665
H1470	32.6667	84.2157	4687
H1480	32.7467	84.2164	4655
H1490	32.8216	84.2668	4818
H1500	32.8946	84.2863	5075
H1510	32.949	84.3047	4964
H1520	33.0271	84.3148	4865
H1530	33.1191	84.221	4660
H1540	33.1935	84.2278	4824
H1550	33.2644	84.2456	4683
H1560	33.3071	84.2464	4584
H1570	33.4219	84.2629	4700
H1580	33.5326	84.2913	4947
H1590	33.6279	84.1707	4830
H1600	33.7501	84.2695	4678
H1610	33.8584	84.2628	4809
H1620	33.9664	84.2234	5100
H1630	34.0654	84.2274	5342

APPENDIX B: SUPPLEMENTARY FIGURES

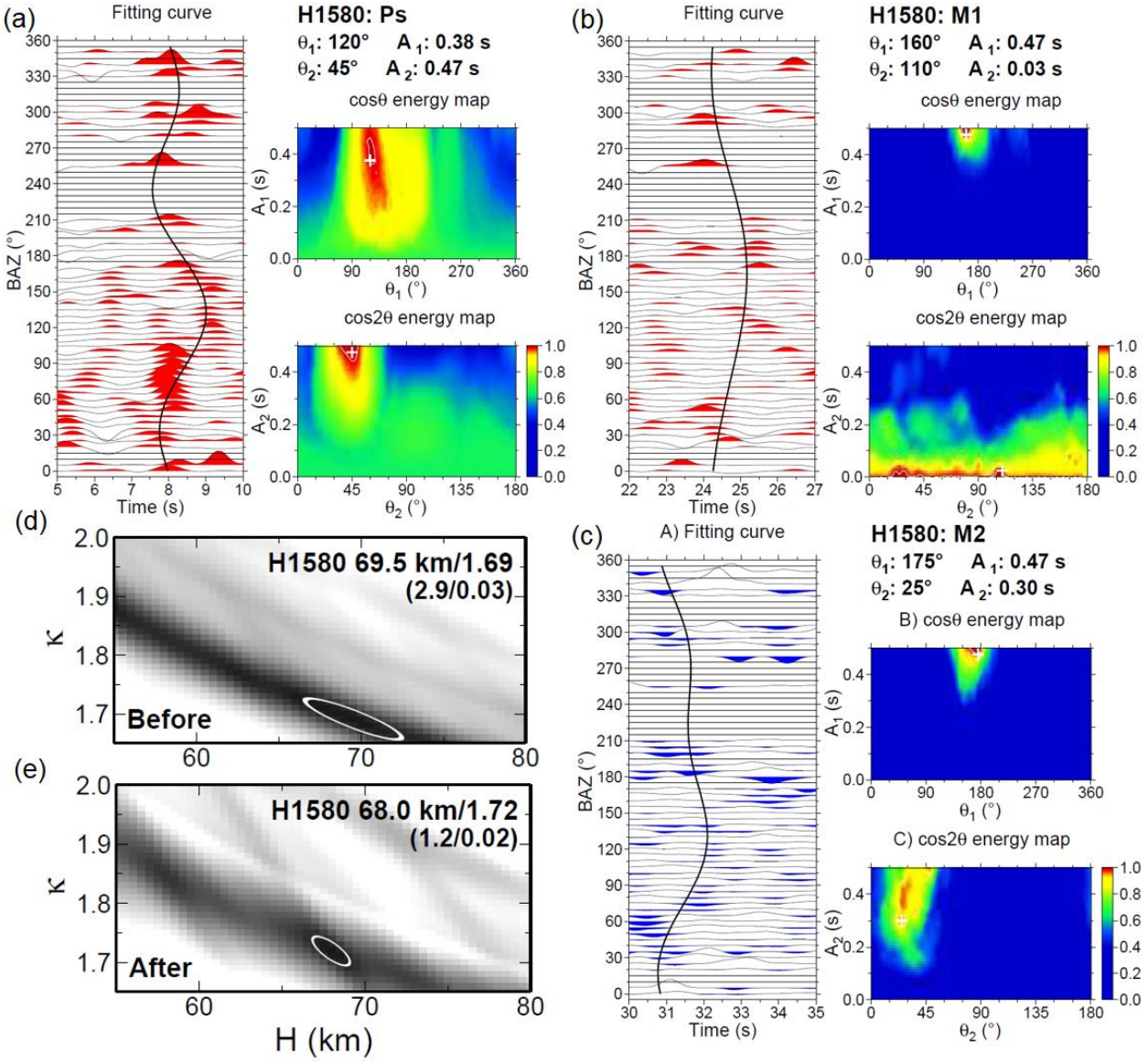

Figure B.1: Harmonic fitting of the arrival times of Ps (a), M1 (b), and M2 (c) in R-RFs of station H1580. (d) is H-κ stacking result before the harmonic correction, and (e) is the result after the harmonic correction. The fitting curve with cosθ and cos2θ functions, energy stacking maps of the grid search for harmonic parameters, and the search results are shown in (a-c). The weighting of phases Ps, M1, and M2 in traditional H-κ method is 0.7, 0.2, 0.1 in (d), and the weighting is 0.5, 0.4, 0.1 in (e).

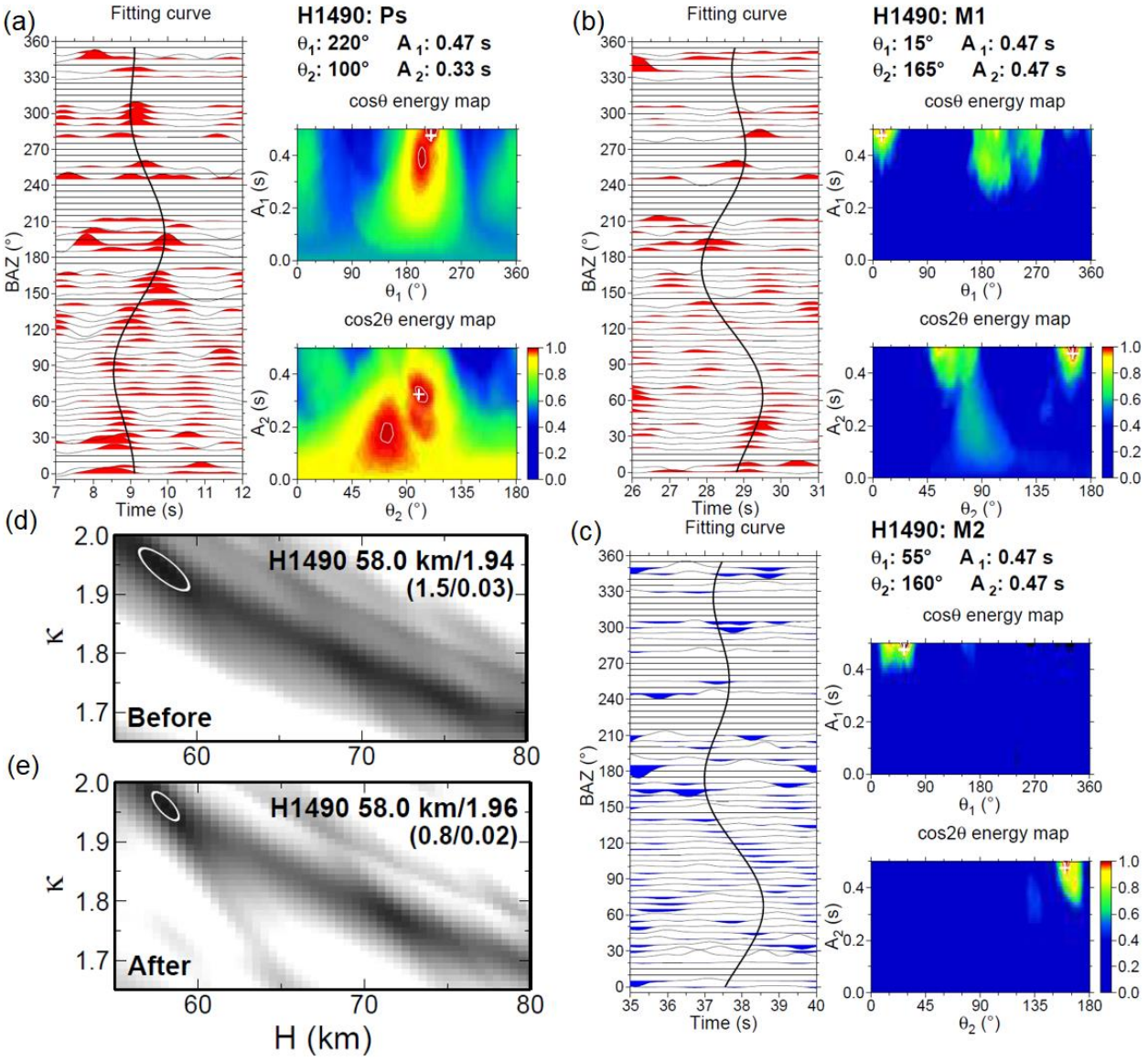

Figure B.2: Harmonic fitting of the arrival times of Ps (a), M1 (b), and M2 (c) in R-RFs of station H1490. (d) is H-κ stacking result before the harmonic correction, and (e) is the result after the harmonic correction. The fitting curve with cosθ and cos2θ functions, energy stacking maps of the grid search for harmonic parameters, and the search results are shown in (a-c). The weighting of phases Ps, M1, and M2 in traditional H-κ method is 0.7, 0.2, 0.1 in (d), and the weighting is 0.5, 0.4, 0.1 in (e).

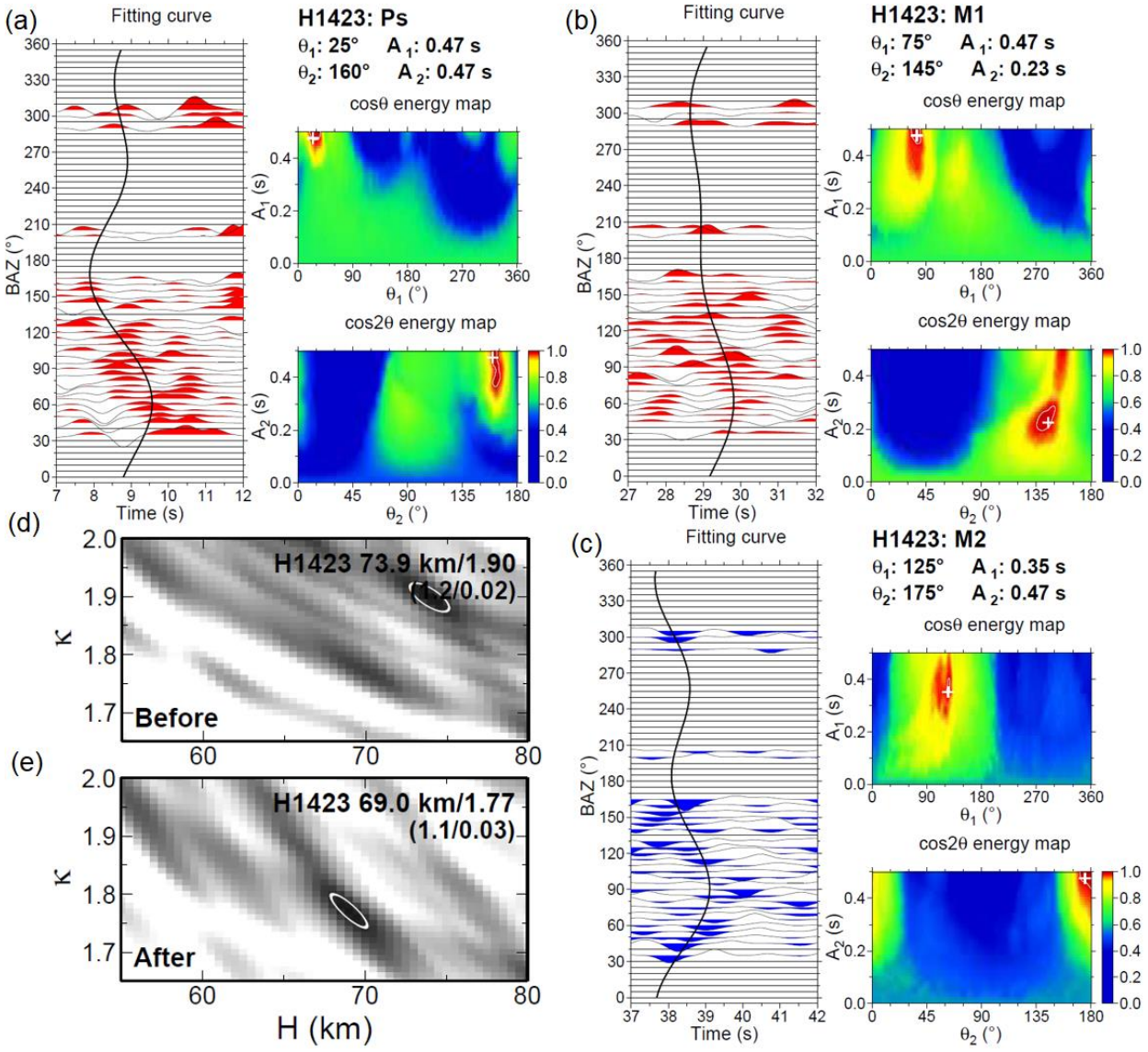

Figure B.3: Harmonic fitting of the arrival times of Ps (a), M1 (b), and M2 (c) in R-RFs of station H1423. (d) is H-κ stacking result before the harmonic correction, and (e) is the result after the harmonic correction. The fitting curve with cosθ and cos2θ functions, energy stacking maps of the grid search for harmonic parameters, and the search results are shown in (a-c). The weighting of phases Ps, M1, and M2 in traditional H-κ method is 0.7, 0.2, 0.1 in (d), and the weighting is 0.5, 0.4, 0.1 in (e).

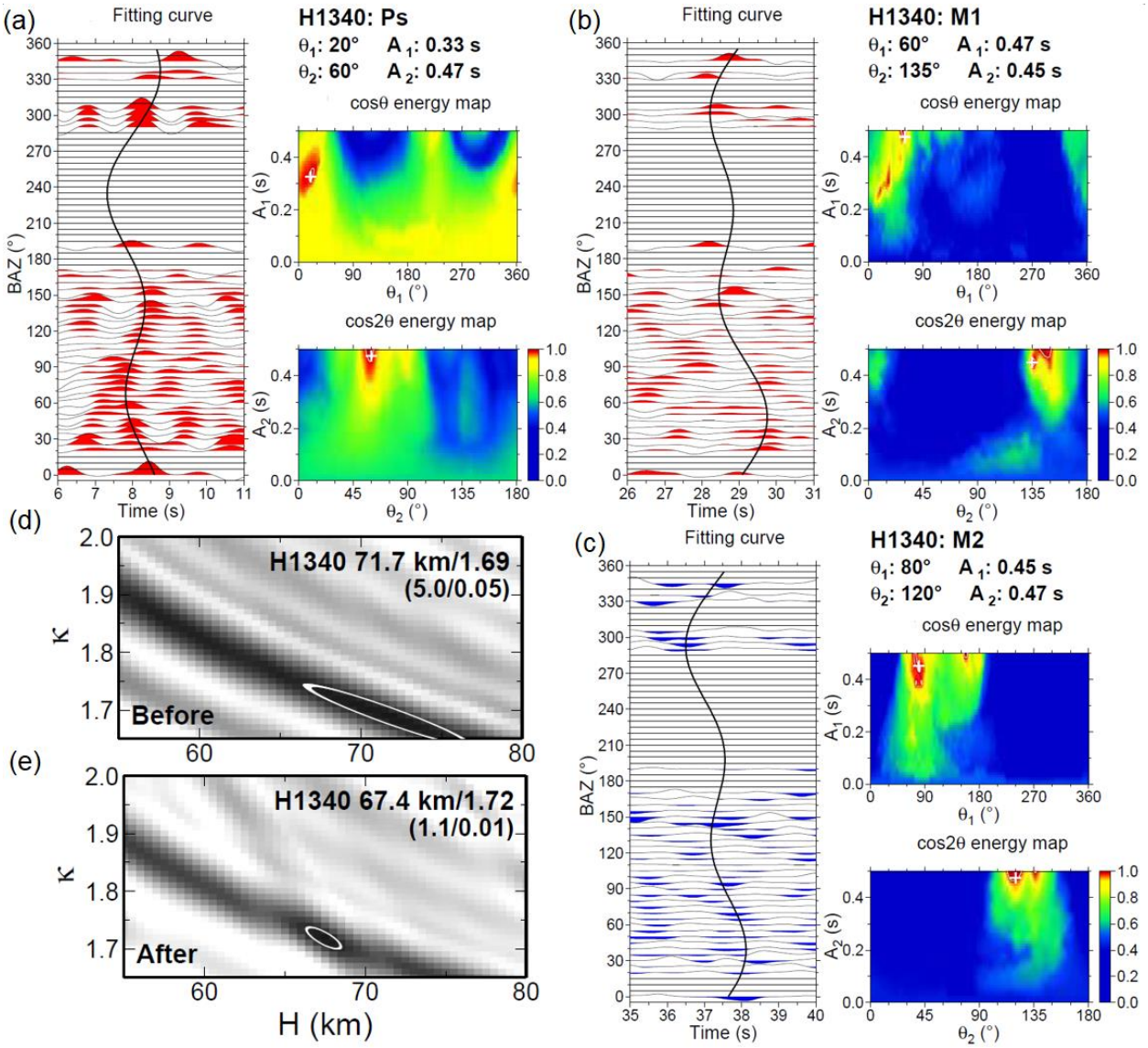

Figure B.4: Harmonic fitting of the arrival times of Ps (a), M1 (b), and M2 (c) in R-RFs of station H1340. (d) is H-κ stacking result before the harmonic correction, and (e) is the result after the harmonic correction. The fitting curve with cosθ and cos2θ functions, energy stacking maps of the grid search for harmonic parameters, and the search results are shown in (a-c). The weighting of phases Ps, M1, and M2 in traditional H-κ method is 0.7, 0.2, 0.1 in (d), and the weighting is 0.5, 0.4, 0.1 in (e).

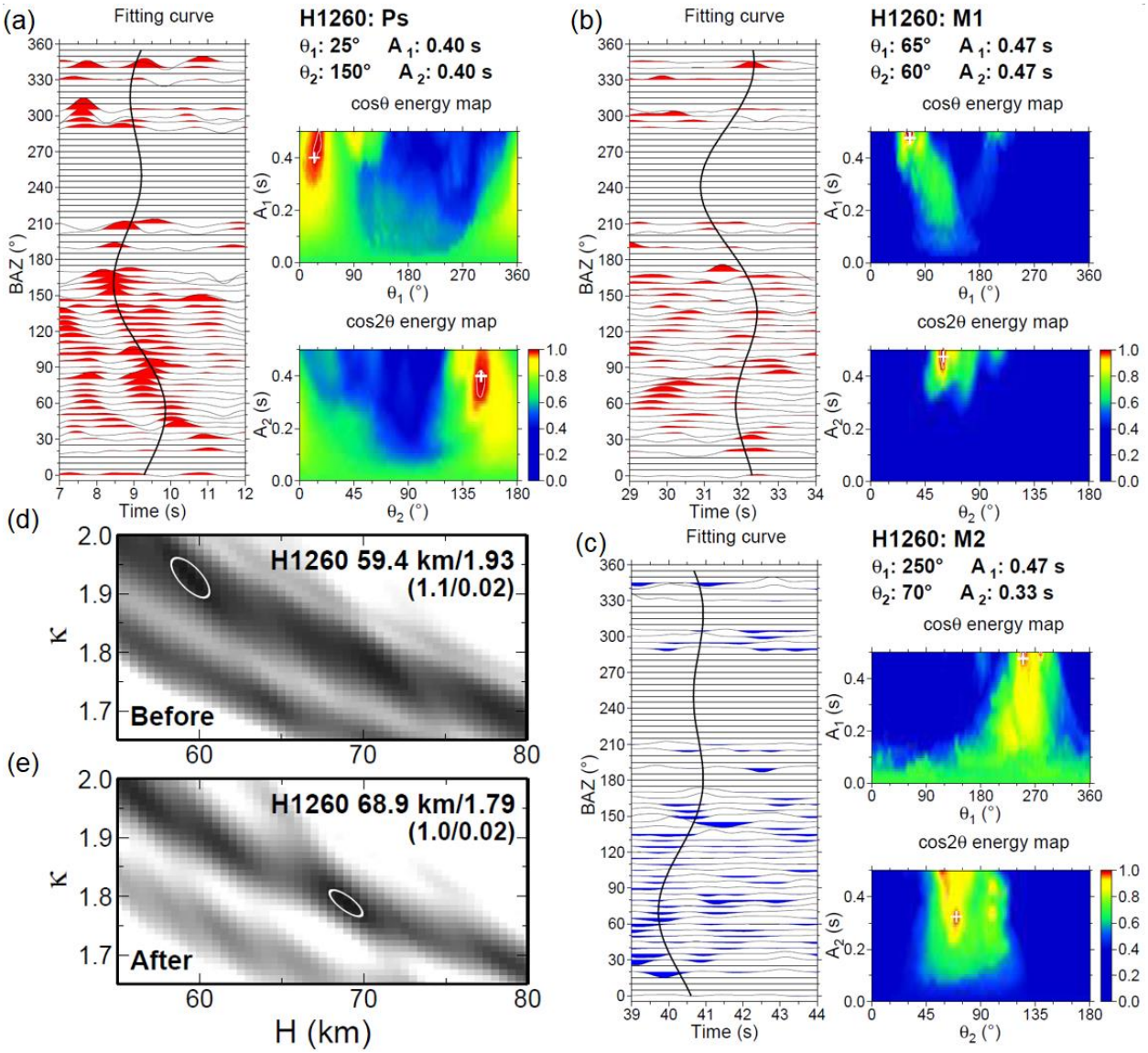

Figure B.5: Harmonic fitting of the arrival times of Ps (a), M1 (b), and M2 (c) in R-RFs of station H1260. (d) is H-κ stacking result before the harmonic correction, and (e) is the result after the harmonic correction. The fitting curve with cosθ and cos2θ functions, energy stacking maps of the grid search for harmonic parameters, and the search results are shown in (a-c). The weighting of phases Ps, M1, and M2 in traditional H-κ method is 0.7, 0.2, 0.1 in (d), and the weighting is 0.5, 0.4, 0.1 in (e).

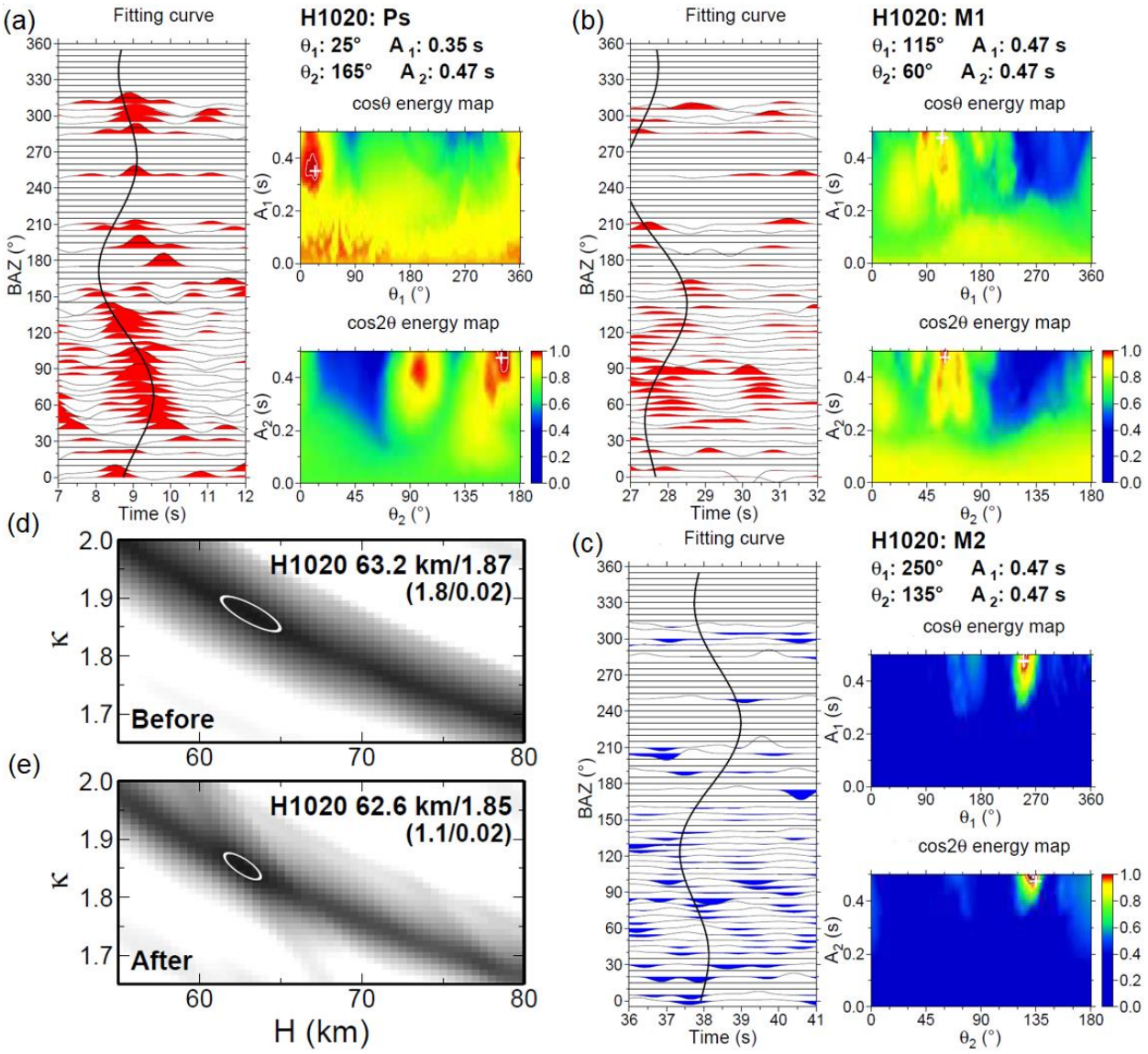

Figure B.6: Harmonic fitting of the arrival times of Ps (a), M1 (b), and M2 (c) in R-RFs of station H1020. (d) is H-κ stacking result before the harmonic correction, and (e) is the result after the harmonic correction. The fitting curve with cosθ and cos2θ functions, energy stacking maps of the grid search for harmonic parameters, and the search results are shown in (a-c). The weighting of phases Ps, M1, and M2 in traditional H-κ method is 0.7, 0.2, 0.1 in (d), and the weighting is 0.5, 0.4, 0.1 in (e).

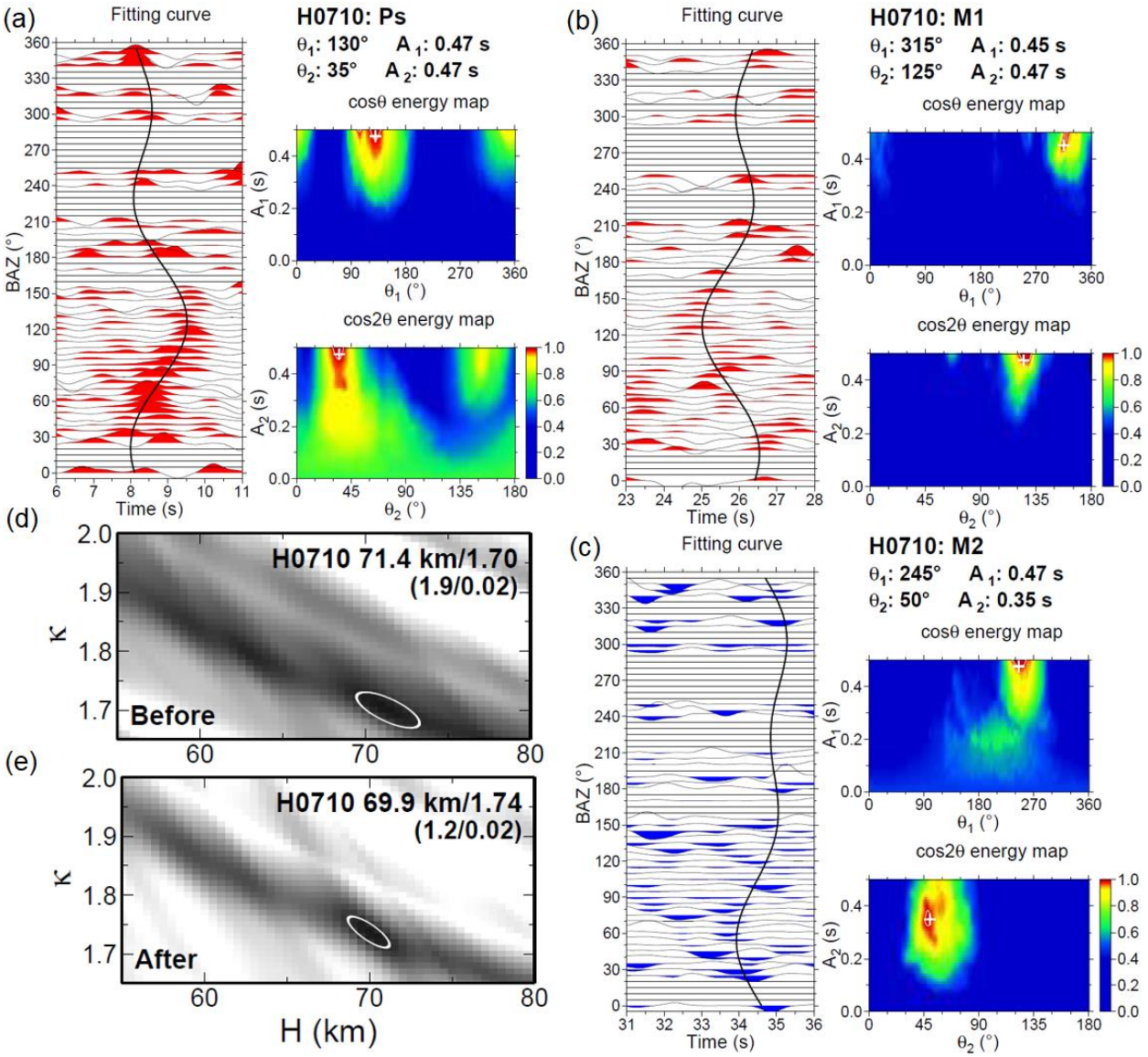

Figure B.7: Harmonic fitting of the arrival times of Ps (a), M1 (b), and M2 (c) in R-RFs of station H0710. (d) is H-κ stacking result before the harmonic correction, and (e) is the result after the harmonic correction. The fitting curve with cosθ and cos2θ functions, energy stacking maps of the grid search for harmonic parameters, and the search results are shown in (a-c). The weighting of phases Ps, M1, and M2 in traditional H-κ method is 0.7, 0.2, 0.1 in (d), and the weighting is 0.5, 0.4, 0.1 in (e).

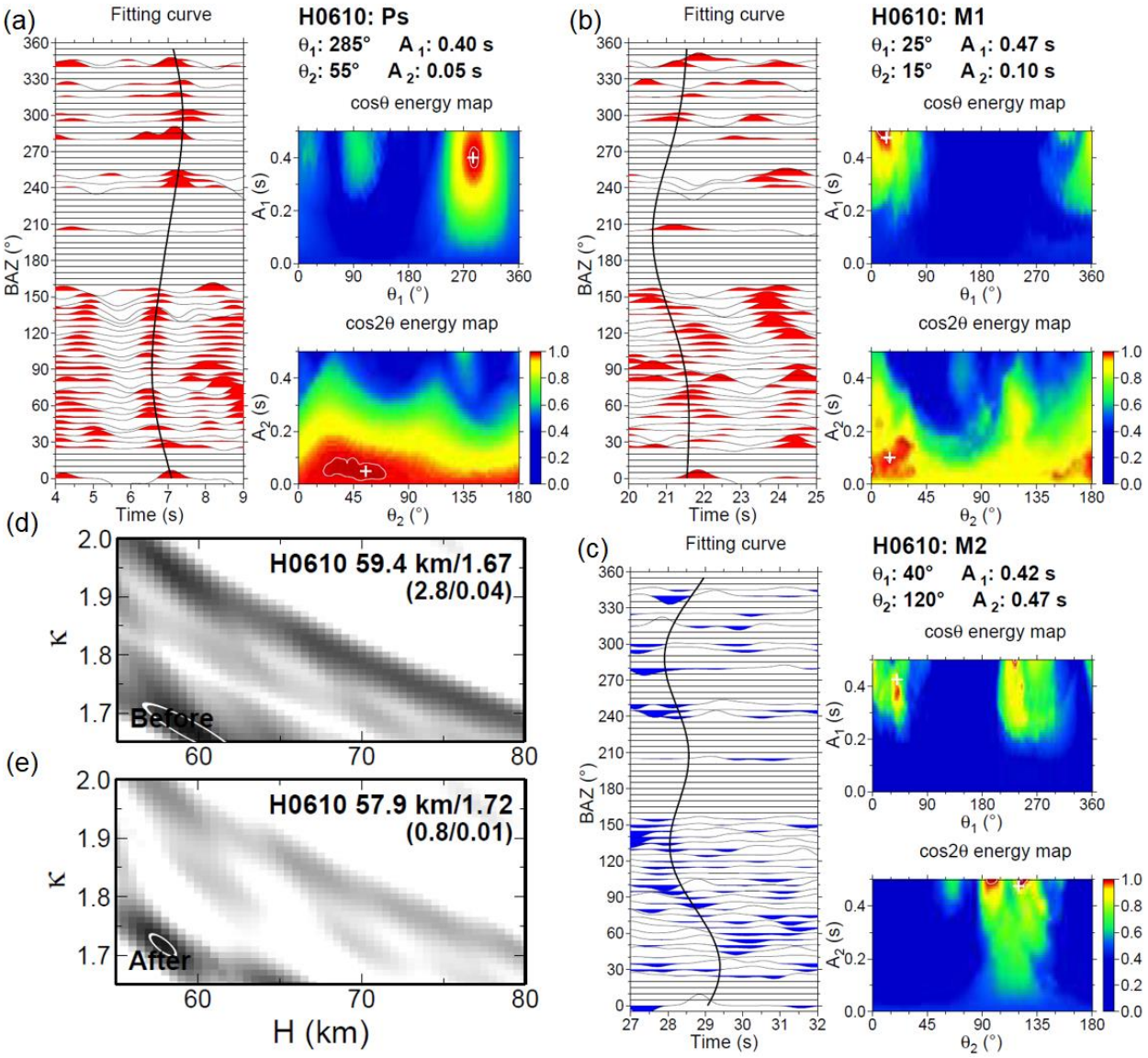

Figure B.8: Harmonic fitting of the arrival times of Ps (a), M1 (b), and M2 (c) in R-RFs of station H0610. (d) is H-κ stacking result before the harmonic correction, and (e) is the result after the harmonic correction. The fitting curve with cosθ and cos2θ functions, energy stacking maps of the grid search for harmonic parameters, and the search results are shown in (a-c). The weighting of phases Ps, M1, and M2 in traditional H-κ method is 0.7, 0.2, 0.1 in (d), and the weighting is 0.5, 0.4, 0.1 in (e).